

Enhanced Mechanical Properties of a Novel High-Nitrogen Cr-Mn-Ni-Si Austenitic Stainless Steel *via* TWIP/TRIP Effects

M. POZUELO, J.E. WITTIG, J.A. JIMÉNEZ, and G. FROMMEYER

Temperature- and strain-rate-dependent mechanical properties of a high-nitrogen austenitic stainless steel containing smaller amounts of nickel than conventional austenitic nickel-chromium stainless steels were investigated with special attention to the formation of martensite or mechanical twins during plastic deformation (TWIP/TRIP effect). After recrystallization treatment at 1050 °C for 0.5 hour, an equiaxed fully austenitic microstructure possessing annealing twins was observed. Tensile tests were carried out at strain rates ranging from 10^{-5} to 10^{-2} s^{-1} in the temperature range from -196 °C to 400 °C. Deformation-induced austenite-to-martensite transformation occurred at temperatures below 0 °C. From room temperature up to 200 °C, plastic deformation is controlled by dislocation glide and mechanical twinning. At temperatures above 200 °C, no deformation-induced structural changes were observed. The formations of bcc α' -martensite and hcp ϵ -martensite, or twins during plastic deformation, were analyzed by optical microscopy, transmission electron microscopy (TEM), and X-ray diffraction.

DOI: 10.1007/s11661-009-9863-8

© The Author(s) 2009. This article is published with open access at Springerlink.com

I. INTRODUCTION

AUSTENITIC stainless steels have been increasingly used in the last 10 years.^[1] These high-performance steels are indispensable in many diverse fields of chemical, marine, and nuclear industries since they conjugate good mechanical properties and excellent corrosion and oxidation resistance.^[2] The fcc austenite structure imparts to the steel greater toughness and formability compared to most common bcc ferritic steels at room temperature. Austenitic steels do not show the ductile-to-brittle transition that ferritic steels show.

There has always been a considerable interest in developing low-cost austenitic stainless steels with similar or improved properties, for instance, replacing nickel with other cheaper alloying elements.^[3–7] In this search for new high-performance austenitic stainless steels with reduced amounts of nickel, manganese is generally considered as the obvious replacement element. However, it is not simply possible to replace nickel by equal amounts of manganese since this element is not as strong an austenite former. Interstitial elements such as carbon or nitrogen must be added to assist in

stabilizing the austenitic structure. It should be noted that a decrease in the Ni content will diminish the corrosion resistance in chloride and fluoride containing aqueous solutions.^[8,9]

In the past 30 years, several austenitic stainless steel grades with low or even without nickel content based on the system Fe-Cr-Mn-N have been developed. These grades include the so-called 200 series.^[10] The austenitic grades completely free of nickel have compositions of the type 17 to 18 pct Cr, 12 to 15 pct Mn, 0.4 to 0.5 pct N, and 0.1 pct C. In general, these steels exhibit at room temperature superior strength, work hardening, and similar ductility compared to Cr-Ni stainless steels.^[11–13] However, most of nickel free stainless steels show a strong increase in yield strength and a severe loss in ductility associated with precipitations of nitrides or carbonitrides during an annealing treatment at temperatures between 600 °C and 900 °C.^[14,15] Thus, the nitrogen content should be reduced to a lower level of <0.35 mass pct and a minimum carbon content of <500 ppm. The decrease in the austenite stability may be compensated with the partial substitution of Ni. These steels would have compositions of the type 16 to 19 pct Cr, 4 to 6 pct Ni, 5 to 10 pct Mn, and 0.25 to 0.35 pct N (mass pct).

An interesting aspect of primarily austenitic stainless steels is associated with the formation of deformation-induced structural changes. The phenomenon of transformation-induced plasticity (TRIP) was thoroughly investigated in steels with large amounts of nickel and chromium.^[16] Austenitic steels containing manganese and large amounts of interstitial elements such as carbon or nitrogen also exhibit strain-induced phase transformation during plastic deformation.^[17–19] Depending on the chemical composition, the stability of the austenite and the stacking fault energy (SFE) may

M. POZUELO, Postdoctoral Student, formerly with the Department of Materials Technology, Max Planck Institut für Eisenforschung, Max Planck Strasse 1, is with the Department of Materials Science and Engineering, University of California, Los Angeles, CA 90095-1595. G. FROMMEYER, Professor, is with the Department of Materials Technology, Max Planck Institut für Eisenforschung, Max Planck Strasse 1, D-04237 Düsseldorf, Germany. Contact e-mail: g.frommeyer@mpie.de J.E. WITTIG, Professor, is with the Department of Materials Science and Engineering, Vanderbilt University, Nashville, TN 37232. J.A. JIMÉNEZ, Postdoctoral Student, is with the Departamento de Metalurgia Física, CENIM, CSIC, 28040 Madrid, Spain.

Manuscript submitted November 12, 2008.

Article published online June 20, 2009

decrease, although with decreasing temperature a decrease in SFE occurs, which promotes martensitic transformation (TRIP effect) or mechanical twinning (TWIP effect) during deformation. In both cases, large elongations to failure and a strong strain hardening will be observed, which are associated with twin and martensite boundaries, which act as effective slip obstacles for dislocation glide.

The purpose of this work was to partially replace nickel in a conventional nickel-chromium stainless steel by manganese and nitrogen in order to reduce the allowing cost and to keep sufficient corrosion resistance by increasing the nitrogen content. In addition, nitrogen and silicon decrease the SFE in austenitic stainless steels. The chosen compositional modification of the chromium-manganese-nickel stainless steel will have a strong influence on the mechanical properties and the strain hardening behavior. The temperature and strain rate dependence of the mechanical properties have been studied in order to evaluate potential applications of this steel. Finally, a systematic study of the microstructure as a function of the plastic deformation in tension tests has been performed to determine the contributions of the strain-induced TRIP and TWIP effects, and dislocation glide mechanisms, to the total deformation.

II. EXPERIMENTAL PROCEDURE

A high-nitrogen austenitic stainless steel of the composition Fe-16.5Cr-8Mn-3Ni-2Si-1Cu-0.25N-0.08Ti ($C \leq 0.05$) (mass pct) was prepared by induction melting in an argon inert gas atmosphere and cast to ingots of 30 mm \times 60 mm \times 200 mm in size. The ingots were hot rolled at 1100 °C to produce strips of about 3 mm in thickness. Final cold rolling was carried out to obtain sheets of about 1.3 mm in thickness. Recrystallization was performed with similar annealing parameters as selected for conventional austenitic stainless steels: 1050 °C/30 min with subsequent water quenching.^[20] After this treatment, the microstructure was evaluated by optical microscopy and X-ray diffraction. For these tasks, the specimens were ground and fine polished with 1- μ m diamond paste and colloidal silica (40 nm) to remove residue from the surface. The grain structure was developed by etching using a mixture of 100 mL H₂O, 100 mL HCl, and 10 mL HNO₃.

The samples for texture analysis were taken from the sheet plane. Texture measurements on the as-cold-rolled and recrystallized sheet material were performed in the back-reflection mode by X-ray diffraction using a X-ray diffractometer setup with a HI-STAR two-dimensional multiwire proportional counter (General Area Detector Diffraction System, Bruker AXS Inc., Karlsruhe, Germany). Co K_α radiation was employed with a tube current of 30 mA and an acceleration voltage of 40 kV. The detector was centered at $2\theta = 55.40$ and 90 deg, coupled with the beam's incident angle θ . At each 2θ position, enough planar frames were collected for covering the entire pole sphere. From the normalized and corrected X-ray data, the two-dimensional (111), (200), and (220) pole figures were reconstructed. The sample

reference system was orthorhombic, corresponding to the symmetry imposed by the rolling process. From these pole figures, the orientation distribution function (ODF) was calculated, using the series expansion method ($l_{\max} = 22$) and ghost corrections. Because austenite possesses cubic symmetry, the orientation density $f(g)$ was represented in the reduced Euler space ($0 \leq \varphi_1, \Phi, \varphi_2 \leq \Pi/2$).

Flat tensile specimens were machined by spark erosion with a gage length of 50 and 10 mm in width according to the German and European standard DIN EN 10 002-1. Tensile samples were cut from the sheet at different angles of 0, 45, and 90 deg to the rolling direction and tested at room temperature with strain rates of $\dot{\epsilon} = 10^{-5}$, 2×10^{-4} , and 10^{-2} s^{-1} . Smaller samples with a 25-mm gage length and 5-mm width aligned parallel to the rolling direction were also cut using spark erosion and deformed in tension as a function of the temperature ranging from -100 °C to 400 °C at a strain rate of $2 \times 10^{-4} \text{ s}^{-1}$.

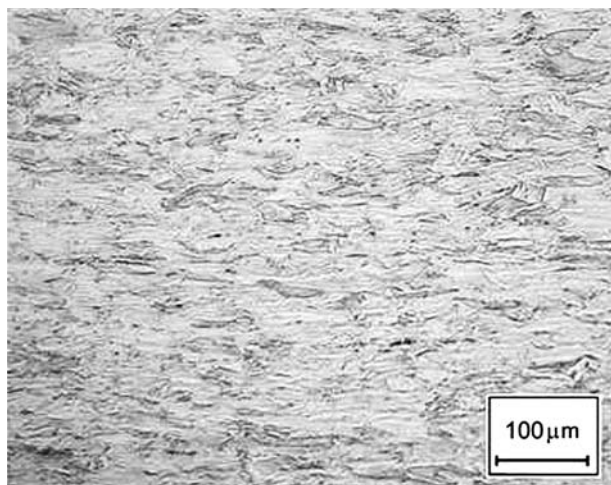
The mechanical properties of high-manganese austenitic steels are strongly dependent on strain-induced deformation and hardening mechanisms such as mechanical twinning and martensitic transformations. In order to gain information about the nature of the strain-induced phase formed during plastic deformation under certain conditions, the grip regions of deformed tensile samples were examined by X-ray diffraction, optical microscopy, and transmission electron microscopy (TEM). In the case of martensite formation, Rietveld refinement was used to determine the volume fraction of the coexisting phases present. The volume fraction of the transformed austenite at -75 °C was determined by interrupted tensile tests at a strain rate of $4 \times 10^{-4} \text{ s}^{-1}$ and at different engineering strains of 15, 30, and 45 pct, respectively.

III. RESULTS AND DISCUSSION

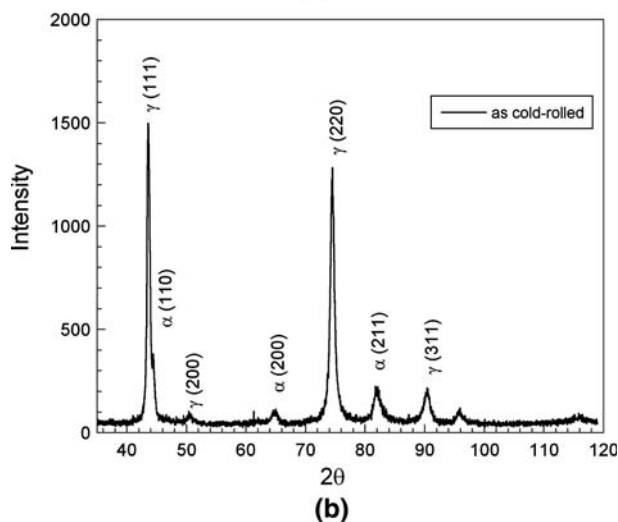
Figure 1(a) shows a representative microstructure present in the rolling plane of the as-cold-rolled strips with a degree of deformation $\eta = 56.6$ pct. The micrograph reveals an elongated grain structure along the rolling direction composed of γ -austenite and α' -martensite, as detected in the X-ray diffraction pattern of Figure 1(b). The volume fraction of each phase determined by Rietveld refinement from this pattern was 75 vol pct austenite and 24 vol pct martensite, respectively. A certain amount of small titanium nitride particles was also observed in the steel. These nitrides appear to be aligned primarily in the rolling direction.

After recrystallization treatment at 1050 °C for 30 minutes and subsequent quenching in water, the microstructure was fully austenitic with equiaxed grains of about 100 μ m containing annealing twins, as shown in Figure 2(a). The absence of martensite in the microstructure was confirmed by X-ray diffraction, as indicated in Figure 2(b).

The ODF plots of the austenite phase after 95 pct cold deformation by rolling are presented in Figure 3(a). The overall texture is a brass-type one, $\{110\} \langle 112 \rangle$, along

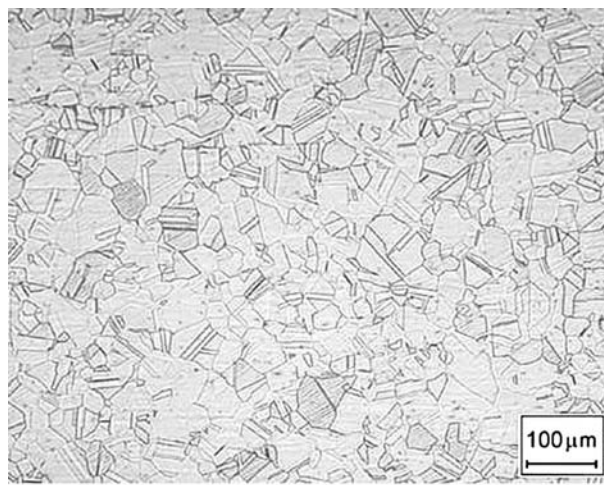


(a)

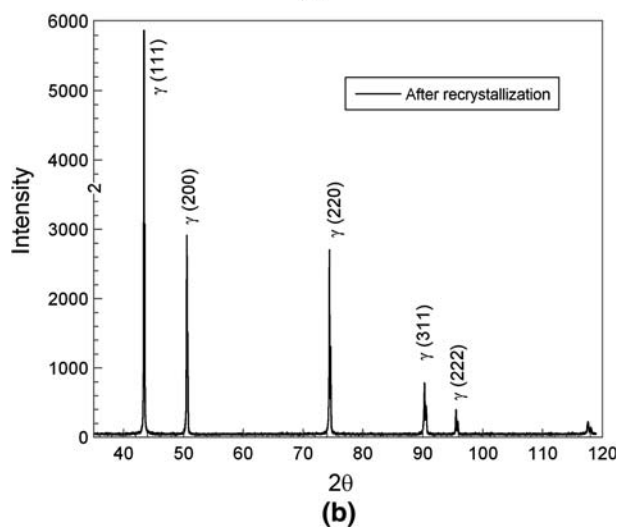


(b)

Fig. 1—(a) Optical micrograph showing the microstructure -longitudinal section- of the as cold rolled high-nitrogen stainless steel sheet, degree of deformation: $\eta = 56.7$ pct. (b) X-ray diffraction pattern of the as cold-rolled sheet revealing the characteristic diffraction peaks of the coexisting γ_{fcc} -austenite and α'_{bcc} -martensite phases.



(a)



(b)

Fig. 2—(a) Optical micrograph showing the microstructure of an as-recrystallized sheet sample consisting of polygonal grains and typical annealing twins of the austenitic matrix. (b) X-ray diffraction pattern of the as-recrystallized sheet showing the typical reflexes of the γ_{fcc} -austenite.

with a scatter toward the Goss orientation, $\{110\} \langle 100 \rangle$. These texture components have been developed during cold rolling of austenitic stainless steels and have been also related to fcc alloys possessing low stacking fault energies. Besides these, the minor $\{112\} \langle 111 \rangle$ component cooper and S, $\{123\} \langle 634 \rangle$, are present in Figure 3(a) at $\phi_2 = 45$ and 65 deg, respectively. After recrystallization at 1050 °C, a randomization of the texture occurred, as presented in Figure 3(b). In this figure, it is observed that only a very weak component $\phi_1\Phi\phi_2 = 70$ deg, 45 deg, 0 and 90 deg equivalent to $\{110\} \langle 221 \rangle$ occurs. This texture component is the P orientation, which is related to the S component of the deformation texture through a 40 deg $\langle 111 \rangle$ relationship.

A. Room-Temperature Mechanical Properties

The standard tensile properties of the as-cold-rolled strips show mechanical anisotropy, specifically the yield

stress, tensile strength, and elongation to failure, that is related to the pronounced texture, as presented in Figure 3(a). Representative engineering stress-strain curves are illustrated in Figure 4(a) for samples deformed at a strain rate of $4 \times 10^{-4} \text{ s}^{-1}$. The three samples exhibit maximum stresses after a few percent of elongations, and no remarkable work hardening occurs. Maximum tensile strength of about 1350 MPa was recorded for the sample with the tensile axis aligned 90 deg to the rolling direction, and the elongation to failure shows a minimum value of about $\epsilon = 9$ pct. Maximum elongation to failure of about $\epsilon = 13.5$ pct was achieved for a sample with the tensile axis aligned 45 deg to the rolling direction, and an ultimate tensile strength of about 1200 MPa was recorded.

The strong anisotropy of the mechanical properties of the as-cold-rolled strips was diminished after recrystallization (1050 °C/ 30 min), as demonstrated by the engineering stress-strain curves of Figure 4(b). This

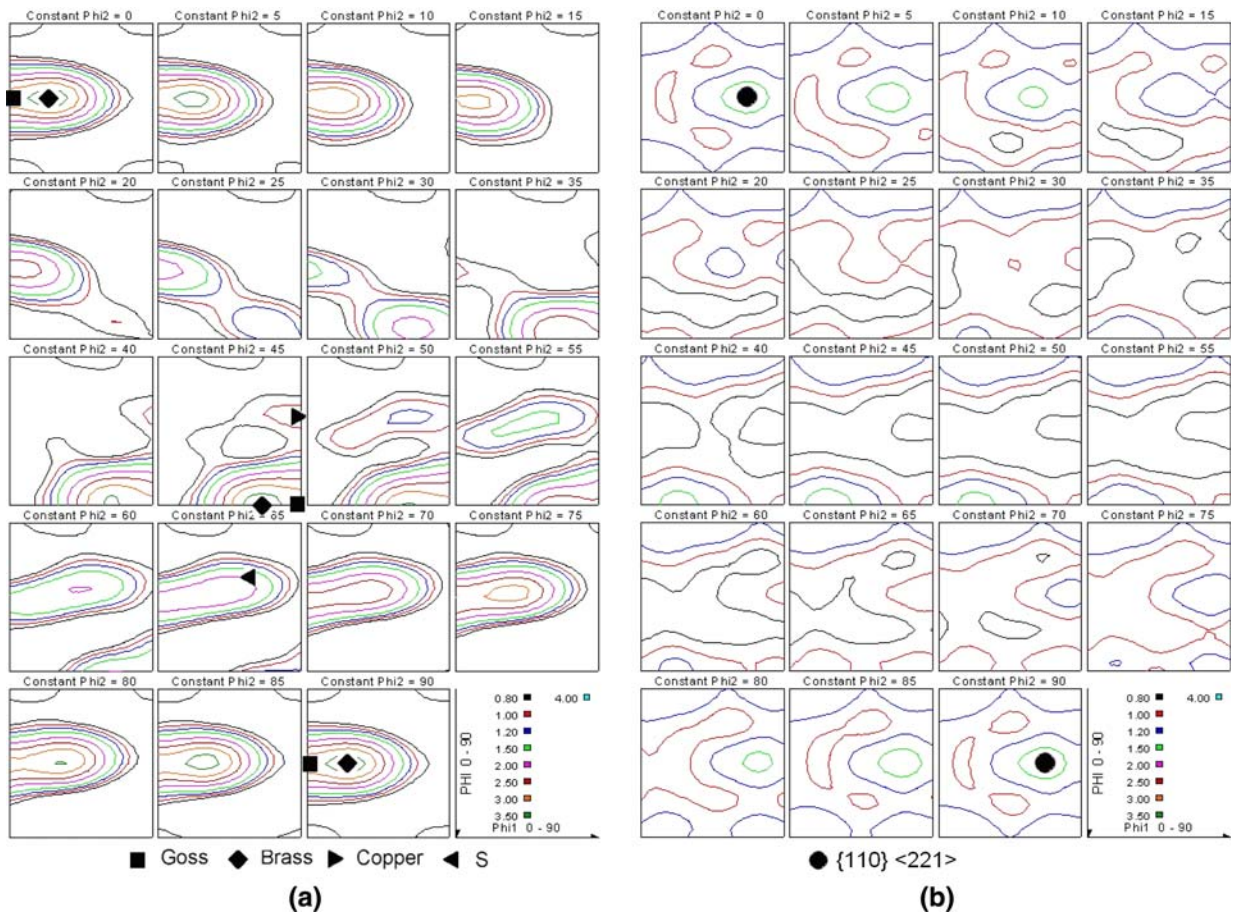


Fig. 3—(a) ODF of the as-cold-rolled steel. ODF is represented as $\varphi_2 = \text{constant}$ sections with $\Delta\varphi_2 = 5$ deg. (b) ODF of the recrystallized steel.

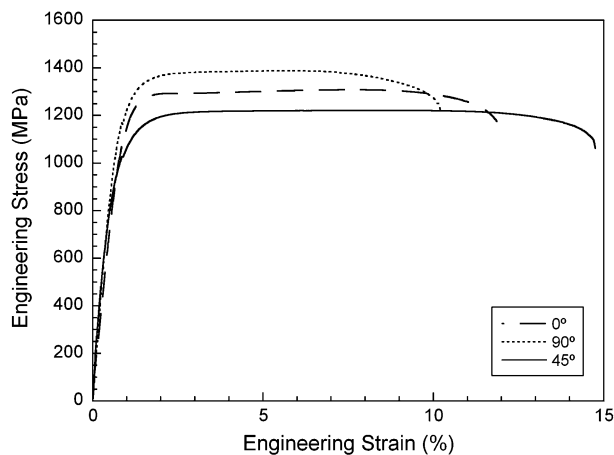
behavior is caused by the random crystal orientations, as shown by the ODF figures in Figure 3(b). The three engineering stress-strain curves presented in Figure 4(b) show similar tensile properties, with yield stresses of 350 MPa and maximum elongations to failure of $\varepsilon > 70$ pct, despite the fact that tensile strength reaches values of greater than 700 MPa. This fact represents an improvement in the mechanical properties of about 30 pct with respect to the strength reported for conventional AISI 304 and 316 stainless steels of 210 and 550 MPa, for the yield stress and tensile strength. The elongation to failure does not exceed 45 to 50 pct, respectively.

Microstructural analysis of a sample tested to failure reveals a large number of thin striations, as shown in Figure 5. However, from this micrograph, it is not possible to differentiate between the substructural features such as twins or martensite. In order to perform a detailed analysis, the sample was examined by X-ray diffraction. Figure 6 shows the X-ray diffraction pattern of a tensile sample, which was strained to failure. The indicated diffraction peaks correspond to γ -austenite, α'_{bcc} -martensite, and ε_{hcp} -martensite. Therefore, the strain-induced α'_{bcc} - and ε_{hcp} -martensites are associated with the TRIP effect.

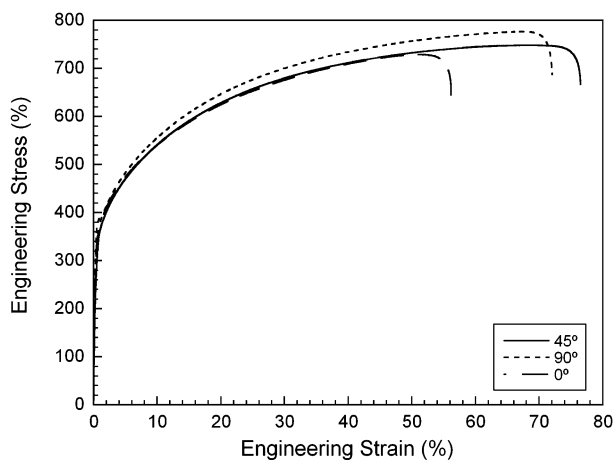
The microstructure from the middle part of the gage length of the tensile samples was also studied by TEM.

The strain to failure produces rather complicated microstructures, which consist of heavily deformed γ_{fcc} -austenite grains with high dislocation densities and deformation-induced α'_{bcc} - and ε_{hcp} -martensite, as shown in Figures 7(a) and (b). Consistent with the results of the X-ray diffraction analysis, the characteristic patterns indicate that austenite is the dominant phase. Because the volume fraction of martensite is relatively low, strain-induced martensite accounts only for a small amount of deformation. In contrast, high dislocation density in γ -austenite accounts for a larger amount of strain, and therefore, the most important deformation mechanism is dislocation glide.

However, this deformation mechanism is of secondary nature, because the high uniform elongations of this steel can be explained by a progressive strain-induced phase transformation during deformation. If local necking occurs at certain points in the gage length, strain-induced martensite will be formed preferentially. Martensite/austenite interfaces act as strong barriers for dislocation glide, and intensive strain hardening takes place in the vicinity of local necks. No further deformation in these strain-hardened regions will occur, but local necking takes place in neighboring areas where the local strains are lower. This repeating process of local necking yields to an extended macroscopic uniform elongation. Therefore, a pronounced work hardening



(a)



(b)

Fig. 4—(a) Engineering stress-strain curves of the as-cold-rolled material from different orientations of the tensile samples; test temperature $\vartheta = 20\text{ }^{\circ}\text{C}$, and strain rate $\dot{\varepsilon} = 2 \times 10^{-4}\text{ s}^{-1}$. (b) Engineering stress-strain curves of the as-recrystallized sheet from different orientations of the tensile samples; test temperature $\vartheta = 20\text{ }^{\circ}\text{C}$, and strain rate $\dot{\varepsilon} = 2 \times 10^{-4}\text{ s}^{-1}$.

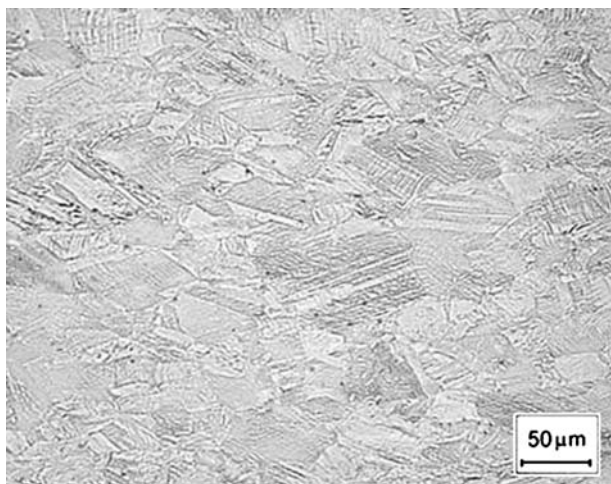


Fig. 5—Microstructure after tensile deformation at room temperature reveals martensite lamellae in the γ -austenite matrix grains.

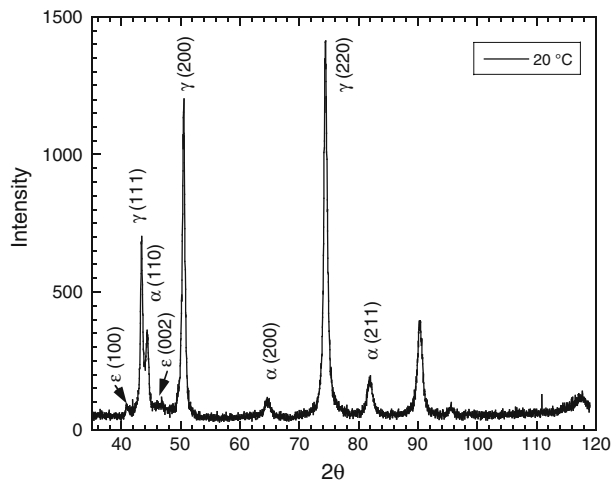


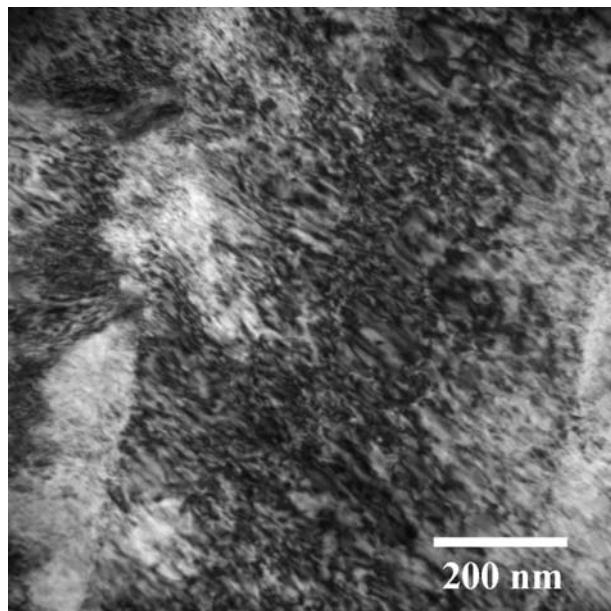
Fig. 6—X-ray diffraction pattern recorded from the region near the fracture of the tensile sample strained at $20\text{ }^{\circ}\text{C}$ showing the characteristic reflexes of the coexisting γ_{fcc} -austenite, ε_{hcp} -martensite, and α_{bcc} -martensite phases.

takes place, as illustrated by the recorded tensile curves of Figure 4(b).

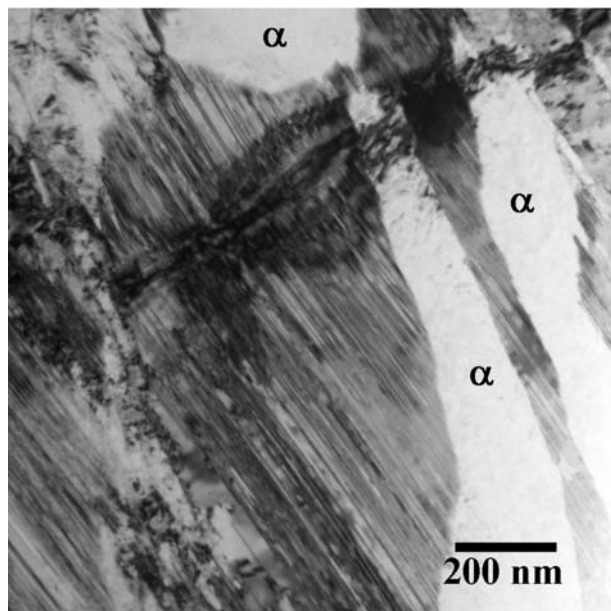
Generally, the amount of strain-induced martensite depends on the temperature and the degree of deformation. Also, the influence of the strain rate on the mechanical properties was investigated in greater detail. Representative engineering stress-strain curves of samples deformed at different strain rates of $\dot{\varepsilon} = 10^{-5}$, 2×10^{-4} , and 10^{-2} s^{-1} are presented in Figure 8. The samples tested at lower strain rates show similar stress-strain curves, whereas samples tested at higher strain rate of 10^{-2} s^{-1} exhibit high yield stresses and lower elongations. This result was expected since the transformation from austenite to martensite suppresses premature necking of the tensile samples according to the formerly described mechanism. Also, high strain rates favor a strong interaction of dislocations with martensite in the sense that large amounts of martensite prevent dislocation glide. Consequently, a pronounced strain hardening and higher flow stresses occur and the uniform elongations to failure of strained tensile samples decrease.

B. Effect of Temperature on the Mechanical Properties

The evolution of the mechanical properties represented by various stress-strain curves as a function of the test temperature ranging from $-100\text{ }^{\circ}\text{C}$ to $450\text{ }^{\circ}\text{C}$ is shown in Figure 9. The X-ray diffraction patterns of the as strained samples tested at temperatures below $20\text{ }^{\circ}\text{C}$ revealed the presence of martensite. This deformation mode is associated with strain-induced martensitic transformation. At test temperatures lower than $25\text{ }^{\circ}\text{C}$, a pronounced change in the curvatures of the engineering strain-stress curves occurs. The strain hardening rate decreases after yielding, but this tendency reverts after a critical amount of strain. The flow stresses increase with increasing test temperature. The pronounced



(a)



(b)

Fig. 7—(a) TEM bright-field image of a tensile sample taken from the as-recrystallized sheet and strained to failure at room temperature, showing an austenite grain with high dislocation density. (b) TEM bright-field image of a tensile sample strained to failure at room temperature, illustrating regions with fine layers of ϵ_{hcp} -martensite and α'_{bcc} -martensite.

progression in the strain hardening rate after the turning point is primarily associated with the $\gamma_{\text{fcc}} \rightarrow \epsilon_{\text{hcp}} \rightarrow \alpha'_{\text{bcc}}$ TRIP mechanism.

The volume fraction of martensite with increasing degree of deformation was stepwise quantified on as-recrystallized tensile samples strained at $\dot{\epsilon} = 4 \cdot 10^{-4} \text{ s}^{-1}$ to engineering strains of $\eta = 15, 30$, and 45 pct at -75°C . The related X-ray diffraction patterns indicated the presence of α'_{bcc} - and ϵ_{hcp} -martensite. The coexisting

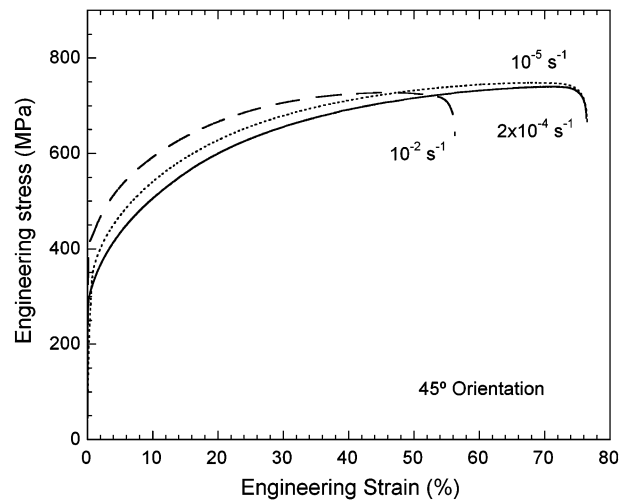


Fig. 8—Engineering stress-strain curves of as-recrystallized tensile samples aligned 45° deg to the rolling direction (RD) recorded at different strain rates.

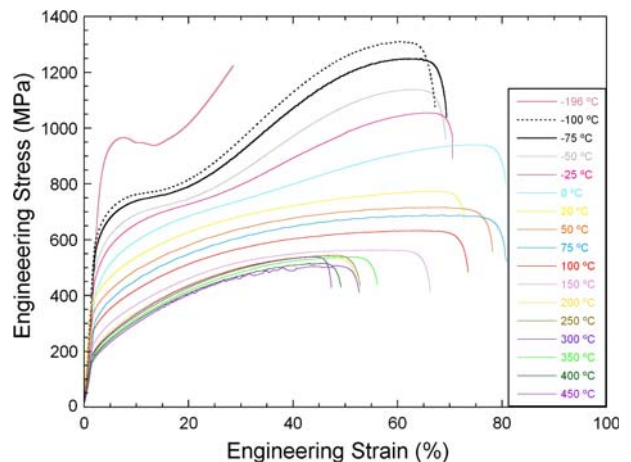


Fig. 9—Engineering stress-strain curves of the as-recrystallized material recorded at different test temperatures ranging from -196°C to 450°C , and strain rate $\dot{\epsilon} = 2 \times 10^{-4} \text{ s}^{-1}$.

phases and their volume fractions as a function of the imposed strain deduced from Rietveld refinement are presented in Table I. The results show that the amount of austenite decreases steadily, whereas at low and medium strains, a considerable amount of ϵ_{hcp} -martensite has been formed. In contrast, the α'_{bcc} -martensite volume fraction increases strongly with increasing strain above $\epsilon = 30$ pct. At the strain to failure of $\epsilon \approx 60$ pct, the total microstructure consists of α'_{bcc} -martensite. However, the amounts of ϵ_{hcp} -martensite are nearly the same at tensile strains of $\eta = 15$ to 30 pct and decrease at higher strains of $\eta \geq 45$ pct to $V_{\epsilon} \leq 5$ pct. From these results, it is concluded that the governing martensite transformation sequence in the investigated stainless steel is $\gamma_{\text{fcc}} \rightarrow \epsilon_{\text{hcp}} \rightarrow \alpha'_{\text{bcc}}$.

Microstructural analysis of a sample tested to failure at -75°C was performed by TEM. Consistent with the results of the X-ray diffraction studies, the microstructure

Table I. Volume Fraction of Austenite and Deformation-Induced α' - and ε -Martensite Determined by X-Ray Diffraction after Tensile Deformation at $-75\text{ }^{\circ}\text{C}$

Engineering Strain as Recrystallized, $\eta = 0$ pct	γ_{fcc} -Austenite 100 Vol Pct	ε_{hcp} -Martensite —	α'_{bcc} -Martensite —
$\eta = 15$ pct	62 vol pct	22 vol pct	17 vol pct
$\eta = 30$ pct	26 vol pct	18 vol pct	56 vol pct
$\eta = 45$ pct	16 vol pct	5 vol pct	79 vol pct
To failure $\eta_f \approx 60$ pct	—	—	≈ 100 vol pct

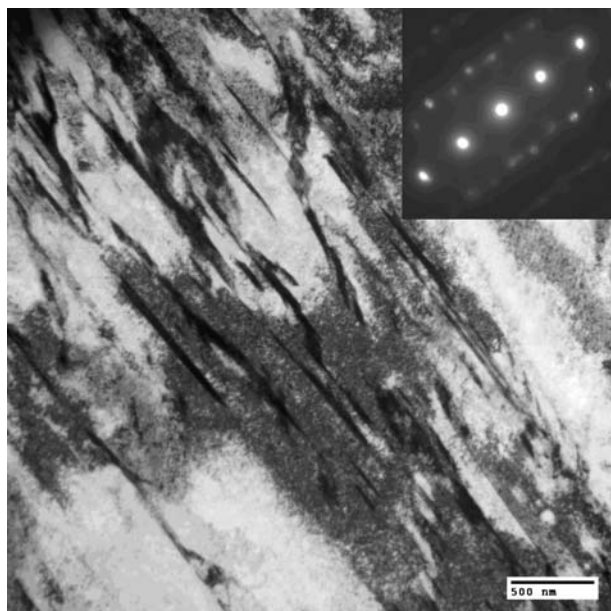


Fig. 10—TEM bright-field micrograph with an inserted diffraction pattern of as-recrystallized tensile sample strained to failure at $-75\text{ }^{\circ}\text{C}$. The image reveals thin layers of ε_{hcp} -martensite.

is essentially transformed to α'_{bcc} -martensite with some retained austenite. However, some small regions of ε_{hcp} -martensite that could not be detected by X-ray diffraction are present, as illustrated in the TEM image of Figure 10.

The variation in the standard tensile properties of the high-nitrogen austenitic stainless steel studied in the temperature range from $-100\text{ }^{\circ}\text{C}$ to $450\text{ }^{\circ}\text{C}$ is illustrated in Figure 11. The shape of the stress-strain curves and the related microstructures of the samples give rise to a classification of the curves into three distinct regions. In the temperature range between $-100\text{ }^{\circ}\text{C}$ and $20\text{ }^{\circ}\text{C}$, a strong increase in the tensile strength with decreasing temperature occurs. This process is accompanied by a slight decrease in the total elongation ε_f from about 80 to 65 pct. The acting TRIP mechanism is related to the instability of austenite and depends also on the stacking fault energy (SFE) of this steel. The SFE dependence on Cr and Ni is well documented in the literature, and the experimental measurements are in good agreement with the thermodynamic models.^[20,21] For the conventional 304 and 316 austenitic stainless steels, the SFE ranges from 9 to 30 mJ/m^2 and from 34 to 80 mJ/m^2 , respectively.^[20]

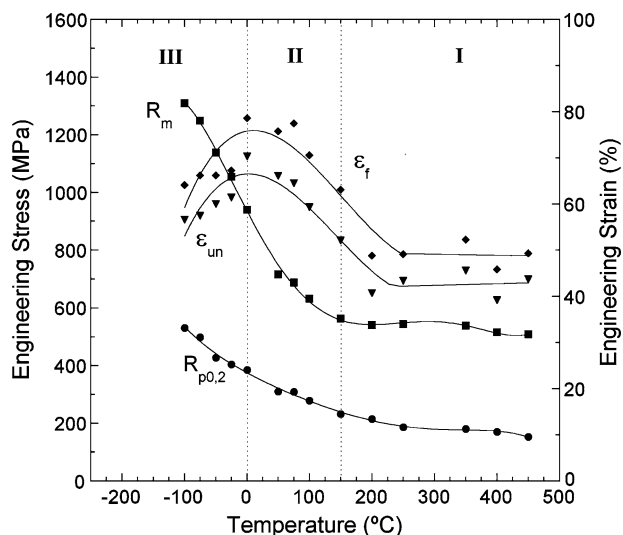


Fig. 11—Tensile properties of the as-recrystallized sheet as a function of the test temperature, and strain rate $\dot{\varepsilon} = 2 \times 10^{-4}\text{ s}^{-1}$. $R_{p0.2}$ —yield stress, R_m —tensile strength, ε_{un} —uniform elongation, and ε_f —elongation to failure.

However, no experimental data on the SFE of the investigated steel are available in the literature. Thus, the SFE was calculated using the thermodynamic regular solution model. A negative Gibbs enthalpy for the martensitic $\gamma_{\text{fcc}} \rightarrow \varepsilon_{\text{hcp}}^{\text{Ms}}$ transformation of $\Delta G^{\gamma \rightarrow \varepsilon} = -164\text{ J/mol}$ and a relatively low stacking fault energy of $\Gamma = 16\text{ mJ/m}^2$ were determined. A stacking fault energy of $<21\text{ mJ/m}^2$ favors the dissociation of $a/2$ [110] dislocations into two $a/6$ [211] partial dislocations and, thereby, the formation of $\varepsilon_{\text{hcp}}^{\text{Ms}}$ martensite (TRIP effect). It is generally believed that the stacking fault energy decreases with decreasing temperature and the formation of strain-induced martensite becomes more favorable. Therefore, the transformation kinetics of austenite to martensite increases and the critical strain for strain-induced martensitic transformation decreases. As a consequence, the elongation to failure decreases and the work hardening rate increases.

In the temperature range from $50\text{ }^{\circ}\text{C}$ to $200\text{ }^{\circ}\text{C}$, a moderate decrease in flow stress, tensile strength, and uniform elongation to failure occurs, as illustrated in Figure 11. X-ray diffraction patterns taken from the deformed region adjacent to the fracture show the presence of peaks corresponding to austenite. The resulting microstructure present in samples deformed at $50\text{ }^{\circ}\text{C}$ consists of slightly elongated grains aligned

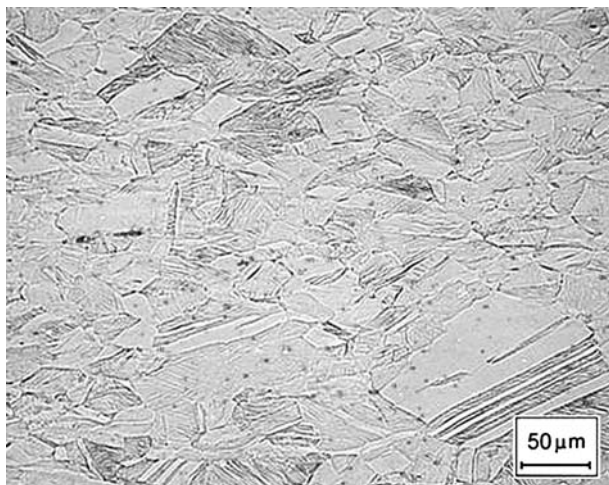


Fig. 12—Optical microstructure of a tensile sample strained to failure at 50 °C, revealing considerable amounts of deformation twins, strain rate $\dot{\epsilon} = 2 \times 10^{-4} \text{ s}^{-1}$.

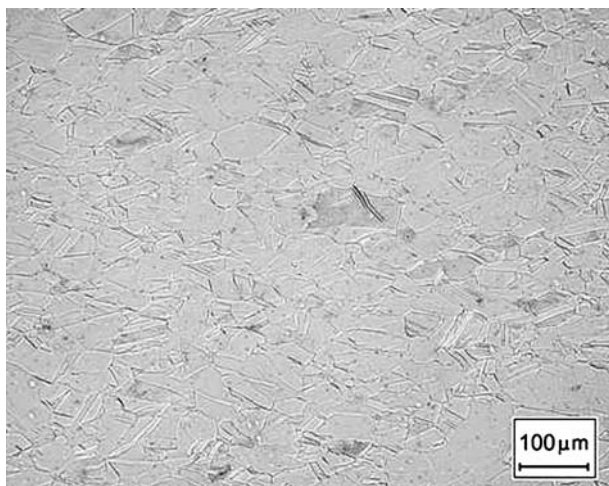


Fig. 13—Optical microstructure of a tensile sample strained to failure at 200 °C, showing less deformation twins due to the increase in stacking fault energy at that temperature, strain rate $\dot{\epsilon} = 2 \times 10^{-4} \text{ s}^{-1}$.

with the tensile direction, which contain a large number of deformation twins, as illustrated in Figure 12. From this, it is concluded that both mechanisms, mechanical twinning and dislocation glide, contribute to total deformation. As the test temperature increases, the formation of mechanical twins becomes less favorable. The microstructure evolution is associated with an increase in stacking fault energy of the austenite, which facilitates the deformation by dislocation glide. A decrease in the density of mechanical twins is accompanied by a decrease in ductility.

At test temperatures ranging from 200 °C to 450 °C, the yield stress, tensile strength, and elongation to failure remain almost constant. The microstructure developed in tensile tests does not exhibit deformation twins except annealing twins inside the grains, as illustrated in Figure 13 for a sample strained to failure

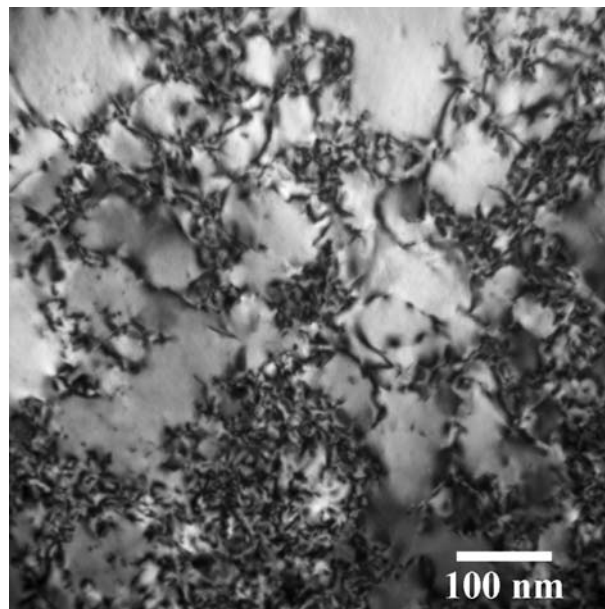


Fig. 14—TEM bright-field image of a sample strained to failure at 200 °C, showing a region with a pronounced dislocation cell structure and localized dislocation tangles.

at 200 °C. Neither deformation twins nor martensite were detected by TEM analysis. The microstructure of the strained tensile sample exhibits an exceptionally high dislocation density, as shown in Figure 14. From this, it is concluded that dislocation glide is the dominant deformation mechanism of the investigated high-nitrogen austenitic stainless at medium temperatures.

IV. CONCLUSIONS

The newly developed high-nitrogen austenitic stainless steel of the composition Fe-16.5Cr-8Mn-3Ni-2Si-1Cu-0.25N-0.08Ti exhibits superior mechanical properties in comparison with conventional austenitic stainless steels. The temperature-dependent mechanical properties are related to specific deformation and strengthening mechanisms of this modified stainless steel.

1. At deformation temperatures ranging from −100 °C to 20 °C, the formation of stress-induced martensite is the dominant deformation mechanism and causes the TRIP effect. The transformation kinetics of austenite to ϵ_{hcp} - and α'_{bcc} -martensite increases as the test temperature decreases. The elongation to failure decreases with increasing work hardening rate.
2. At temperatures ranging from 50 °C to 200 °C, accompanying deformation mechanisms such as mechanical twinning and dislocation glide contribute to total deformation. Maximum elongations to failure were achieved due to the TWIP effect. As the test temperature is increased, the formation of mechanical twins during deformation becomes less favorable. This is caused by an increase in the stacking fault energy. The decrease in the formation

rate of mechanical twins is accompanied by a decrease in ductility.

3. At temperatures ranging from 200 °C to 450 °C, the yield stress, the tensile strength, and the elongation to failure remain almost constant. In this case, dislocation glide is the dominant deformation mechanism.

ACKNOWLEDGMENTS

The financial support of the present work by the Comisión Interministerial de Ciencia y Tecnología under Grant No. MAT2006-13348 is acknowledged. One author (MP) is grateful for the financial support through a “Fulbright” scholarship by the Fulbright Program and Spanish Ministry of Education and Science.

OPEN ACCESS

This article is distributed under the terms of the Creative Commons Attribution Noncommercial License which permits any noncommercial use, distribution, and reproduction in any medium, provided the original author(s) and source are credited.

REFERENCES

1. S. Malm and T. Pauly: *5th Eur. Stainless Steel Science and Market Congr.*, Sevilla, Sept. 27–30, 2005, pp. 11–16.

2. P.J. Cuna: *The Euro Inox Handbook of Stainless Steel*, Euro Inox Publications, Brussels, 2002, pp. 1–86.
3. S.K. Banerji: *Met. Progr.*, 1978, vol. 113 (4), pp. 59–62.
4. G.T. Haddick, L.D. Thompson, E.R. Parker, and V.F. Zackay: *Met. Progr.*, 1978, vol. 114 (6), pp. 37–40.
5. J. Demestre, R. Leveque, and A. Mercier: *Rev. Metall. Paris*, 1970, vol. 67, pp. 399–412.
6. J.C. Garcia, N. Rosas, and R.T. Rioja: *Met. Progr.*, 1982, vol. 122 (3), pp. 47–50.
7. R. Wang and F.H. Beck: *Met. Progr.*, 1983, vol. 123 (4), pp. 72–76.
8. C.R. Clyton and I. Olefjord: in *Corrosion Mechanism in Theory and Practice*, P. Marcus and J. Quadar, eds., Marcel Dekker, New York, NY, 1995, pp. 175–99.
9. G. Herting, I. Odnevall Wallinder, and C. Leygraf: *Corr. Sci.*, 2007, vol. 49, pp. 103–11.
10. J. Charles: *5th Eur. Stainless Steel Science and Market Congr.*, Sevilla, Sept. 27–30, 2005, pp. 19–27.
11. E. Werner: *Mater. Sci. Eng. A*, 1988, vol. 101, pp. 93–98.
12. R.P. Reed: *J. Met.*, 1989, vol. 41, pp. 16–21.
13. M.O. Speidel and R.M. Pedrazzoli: *Mater. Performance*, 1992, vol. 31, pp. 59–61.
14. J.W. Simmons: *Metall. Mater. Trans. A*, 1995, vol. 26A, pp. 2085–2101.
15. H. Chandra Holm, P.J. Uggowitzer, and M.O. Speidel: *Scripta Metall.*, 1987, vol. 21, pp. 513–18.
16. L. Remy: *Acta Metall.*, 1978, vol. 26 (7), pp. 443–51.
17. G. Frommeyer, U. Brück, and P. Newman: *ISIJ Int.*, 2003, vol. 43, pp. 438–46.
18. F. Chen, P. Li, S. Chu, and C. Chou: *Scripta Metall.*, 1991, vol. 25, pp. 585–90.
19. Q. Dai, R. Yang, and K. Chen: *Mater. Characterization*, 1999, vol. 42, pp. 21–26.
20. G.B. Olson and M. Cohen: *Metall. Trans. A*, 1976, vol. 7A, pp. 1897–1904.
21. P.J. Ferreira and P. Müllner: *Acta Mater.*, 1998, vol. 46, pp. 4479–84.
22. A.F. Padilha, R.L. Plaut, and P.R. Rios: *ISIJ Int.*, 2003, vol. 43, pp. 135–43.